Proceedings of the 21st ICSMGE, Vienna, Austria, 14 – 19 June 2026. Pistrol, Adam & Schweiger (eds.)
Published by: ÖGG, Austrian Society for Geomechanics, Salzburg, Austria, ISBN 978-3-9503898-4-5
https://doi.org/10.53243/ICSMGE2026-221

Pore structure evolution of coral gravel during particle breakage: a multi-scale investigation

Xianwei Zhang
State Key Laboratory of Geomechanics and Geotechnical Engineering Safety, Institute of Rock and Soil Mechanics, Chinese Academy of Sciences, Wuhan, China

Lei Yan, Hualiang Zhu
State Key Laboratory of Geomechanics and Geotechnical Engineering Safety, Institute of Rock and Soil Mechanics, Chinese Academy of Sciences, Wuhan, China;
University of Chinese Academy of Sciences, Beijing, China, yanlei231@mails.ucas.ac.cn

ABSTRACT: Coral gravel soil, coral sand, and coral-derived mixed soil are commonly found in coastal regions and islands, where biologically formed, fossilized sediments, such as coral gravel (CG), are abundant. The unique pore characteristics and irregular shapes of CG particles contribute to their high porosity and significant susceptibility to breakage, which notably influence their mechanical and physical properties. However, the mechanisms driving the evolution of pore structures in CG during particle breakage are not yet fully understood. This study employs a multi-scale analytical approach, combining X-ray computed tomography and structural simulations, to investigate changes in pore structure across four distinct types of CG—rod-shaped, branchlet, massive, and flaky—during particle fragmentation at different volume scales. The results show that the internal pores of the particles can be classified into intraparticle, blind, and through pores. As breakage progresses, intraparticle and blind pores decrease, while through pores increase. Specifically, as the degree of particle breakage increases, the transformation between pore types becomes more pronounced. In the branchlet and flaky CG samples, relative intraparticle porosity decreases from 74.43% and 72.88% to 22.32% and 12.2%, respectively, while relative blind and through porosity increase significantly as fragmentation intensifies. This study provides a framework for understanding the evolution of pore structure during particle breakage by analyzing variations in porosity, thus advancing our knowledge of the pore structures of brittle granular materials. The findings offer valuable insights for the design and performance evaluation of biological materials in coastal and geotechnical engineering applications.

KEYWORDS: Coral gravel, pore structure, porosity, particle fragmentation, X-ray microcomputed tomography.

1 INTRODUCTION

Coral gravel (CG), with its biological origin and complex depositional environment, exhibits irregular particle shapes, well-developed pore structures, and a high potential for breakage (Ding et al. 2021; Zhang et al. 2022), distinguishing it from conventional terrestrial soils. Employing Computed Tomography (CT) scanning and digital image processing techniques, Lyu (2019) has shown that CG particles can display up to 40% internal porosity levels. This high internal porosity categorizes CG as a brittle porous geomaterial, which decreases particle strength and enhances the potential for breakage (Shen et al. 2020). Compared to siliceous materials commonly utilized in geotechnical engineering, CG, predominantly comprising calcium carbonate, demonstrates lower hardness and strength, making it more susceptible to degradation and fragmentation under compressive or shear stress (Coop et al. 2004). During particle fragmentation, external forces cause stress to concentrate at particle contact points or internal defects, initiating and propagating cracks. However, the specific changes in the pore structure of CG during particle fragmentation remain poorly clarified, and the classification of pore types, along with their distinct functional roles at the pore level, are not fully understood. Thus, developing advanced and rigorous microstructural characterization methods is highly recommended to accurately capture the dynamic evolution of pore structure during particle fragmentation, which is difficult to observe with the naked eye and conventional imaging techniques.

Researchers have defined several parameters to quantify the pore features of brittle geomaterial particles, including porosity and diameter. They have used mercury intrusion porosimetry and the gas adsorption method to measure porosity and pore volumes through intrusion volume analysis and computational geometry based on 2D projections of geomaterial particles (Clarkson et al. 2013; Ouellet et al. 2007). However, both testing methods, which rely on gas or liquid intrusion, struggle to measure closed pores within particles accurately and can damage the internal pore structure under high intrusion pressures, inhibiting the reproducibility of the results. Understanding the evolution of three-dimensional (3D) pore structures and hydraulic properties in CG during particle fragmentation remains limited. Fortunately, X-ray computed tomography (X-CT), a novel nondestructive 3D imaging technique, offers a more reliable alternative to traditional methods (Ni et al. 2017). This technique provides high spatial resolution and complete 3D information, which has been employed to investigate the internal porosity characteristics and pore distribution of individual CS particles (Fan et al. 2021). However, these applications of CT technology do not provide insights into the pore structure changes of CG, especially when considering multi-scale simulations of particle fragmentation.

In response to the issues described, this study implements a multi-scale concept to assess the dynamic evolution of pore structure of CG during particle fragmentation. Utilizing X-ray computed tomography (X-CT) scans, this method generates 3D rendering models of the microscopic pore structures and their digital information of CG at various simulation volume scales, enabling a comprehensive analysis of both the qualitative and quantitative evolution of internal pores. In addition, multi-scale simulations provide insights into the mechanisms of pore evolution during particle breakage. The study offers new insights into the pore structure of CG and presents effective methods for predicting these characteristics.

2 MATERIALS AND METHODS

2.1 *Sample preparation*

The coral gravel analyzed in this study was collected from a construction site in Yulin Bay, Sanya City, located in Hainan Province, China. The mineralogical and elemental compositions of CG were determined using X-ray diffraction (XRD) and energy-dispersive spectroscopy (EDS), revealing that it consists of approximately 96% aragonite ($CaCO_3$) and 4% calcite ($CaCO_3$). Based on the previous findings （Zhang et al. 2022), which revealed that the fragmentation potential of CG is strongly influenced by morphological factors such as particle roughness, size, and microstructure, this study selected four typical types of CG samples with distinct particle morphologies and structural characteristics to evaluate the impact of sample shape on subsequent simulations. The photographs of these four typical CG samples, labeled from C1 to C4, are presented in Figure 1: (i) Sample C1: the rod-shaped CG, resembling a solid cylinder with small pores visibly present on the surface, attributed to its biological origin; (ii) Sample C2: the branchlet CG, resembling a small branch with a complex structure characterized by multiple branched formations featuring protrusions and depressions; (iii) Sample C3: the massive CG, which is distinguished by large hollow cavities and isolated surface holes; (iv) Sample C4: the flaky CG, characterized by a flaky appearance. The surface exhibits a pronounced calcareous cementation, reflecting the properties of CG as $CaCO_3$.

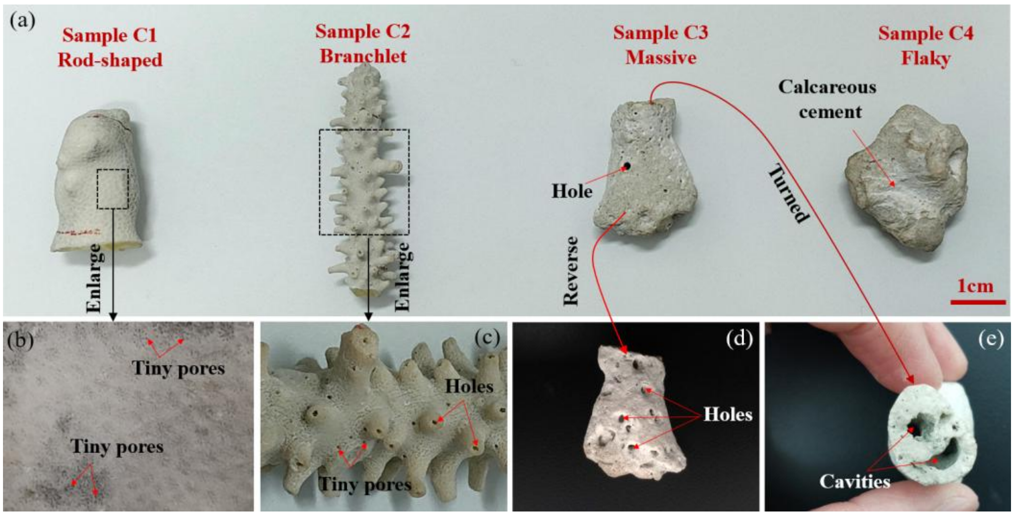

Figure 1. Morphology and enlarged images of different types of CG.

2.2 *X-CT scanning tests*

This study first conducted a non-destructive X-CT scanning experiment on the CG sample to accurately capture its structure to analyze the particle morphology and pore structure characteristics of CG in different forms. The X-CT scanning test was conducted using the Xradia 410 Versa instrument, which has an optimal resolution of 0.1 μm and comprises three main components: an X-ray source, a turntable system, and an X-ray detector. During the test, X-rays emitted by the X-ray source passed through the test sample placed on the turntable before reaching the X-ray detector. The detector transmitted the captured data to a computer system, which processed it into high-resolution grayscale images.

2.3 *Pore structure analysis*

These images were reconstructed into 3D structures through slice stacking using the specialized image analysis software AVIZO. Due to the varying grayscale thresholds of different structures resulting from differences in density, this study applied a multi-threshold segmentation algorithm and a connectivity analysis algorithm to process the grayscale images obtained from X-CT scanning. Then, 3D digital models of different pore types were reconstructed using the software (Section 2.5 for pore classification). In addition, the particle analysis module in the software was employed to quantitatively analyze equivalent pore diameter and porosity to assess their effects on the fragmentation characteristics of CG particles.

2.4 *Multi-scale analysis method*

Due to the structural collapse during particle breakage, real-time measurement of changes in the microscopic pore characteristics of CG samples through standard compression tests is impractical for investigating particle fragmentation. This study proposed a multi-scale method to simulate particle breakage, facilitating observing pore structure evolution during fragmentation. Initially, the particles were reduced to smaller pieces during fragmentation, gradually decreasing the volume of individual fragments. A series of models were developed using CT scans to simulate the volume change of individual pieces during particle fragmentation. These models represent the original sample volume along with one-quarter (1/4), one-ninth (1/9), and one-sixteenth (1/16) of that volume, reflecting the gradual fragmentation of CG. In addition, smaller fragment modules were selected from larger ones to ensure continuity in the breakage analysis, as illustrated in Figure 2. The pore structures of each fragment module were then analyzed based on the steps outlined in Section 2.3.

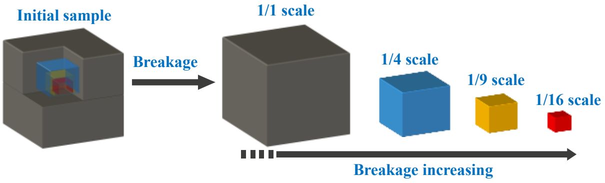

Figure 2. Multi-scale analysis simulates particle breakage.

2.5 *Pore classification*

Various methods have been adopted by researchers, with the IUPAC (1994) classification being the most widely used to systematically classify pore characteristics. Based on this classification, CG pores are divided into three categories based on their interaction with external fluids, as shown in Figure 3. The first category comprises isolated intraparticle pores, which are not connected to external fluids and are typically located within individual CG particles. The second category includes blind pores, which are accessible from one side but do not extend through the entire particle. The third category consists of through pores, which create continuous pathways connecting the particle to external fluids at both ends, as observed in the cavities of massive CG particles in Figure 1.

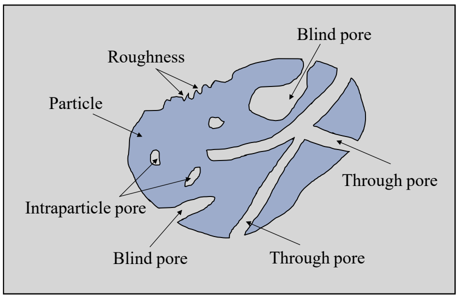

Figure 3. Schematic diagram of particle pore classification.

Following this classification, quantitative data such as pore volume and equivalent diameter are generated. This information is pivotal for elucidating the particles' porosity and structural integrity. Quantifying the volumes of intraparticle, blind, and through pores, denoted as V_i, V_b, and V_t, respectively. The total pore volume V_v is the sum of V_i, V_b, and V_t. Correspondingly, the porosities are represented as ϕ_i, ϕ_b, ϕ_t, and ϕ_v, respectively, with the relative porosities denoted as f_i, f_b, and f_t. In addition, the equivalent pore diameter D, utilized to quantify pore size, is calculated following Equation (1), where A is the area of the pore.

$$D = \sqrt{\frac{4A}{\pi}} \tag{1}$$

3 RESULTS AND ANALYSIS

3.1 *Pore morphological characteristics*

This research obtained assorted 3D pore distribution images (Figure 4) from CT scans to examine and contrast the pore morphology across different CG types. Figure 4 shows that the rod-shaped CG (C1) includes a through pore that vertically penetrates the entire sample, encircled by numerous small intraparticle pores. In addition, the surface features numerous small blind pores, which correlate closely with the visual characteristics depicted in Figure 1. The branchlet CG (C2) exhibits a branching, dendritic morphology, with pores scattered along its protruding branches. In addition to the scattered nature of the intraparticle pores, the 3D pore distribution image emphasizes that these pores are predominantly small and isolated, exhibiting low connectivity between branches. The 3D image further verifies the absence of a through pore in C2. In contrast, the massive CG (C3) displays prominent and well-developed through pores. The 3D image demonstrates that the through pores in C3 possess the largest volume among all CG types, with evident vertical and horizontal connectivity. In addition, the inward-sunken depressions on its surface (Figure 1) indicate a relatively larger volume of isolated blind pores compared to other CG types. Flaky CG (C4) pore characteristics include more prominent and isolated blind and intraparticle pores than in other CG types. The 3D image reveals that the intraparticle pores are primarily situated within the core of the sample, with no visible through pores.

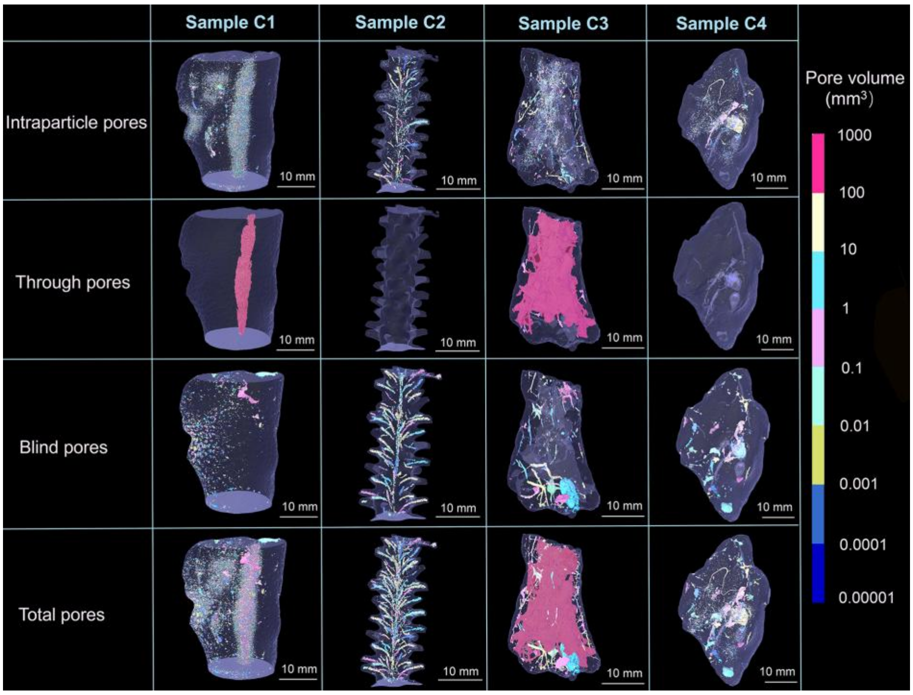

Figure 4. Various 3D pore distribution images of CG.

The pore structures of CG demonstrate apparent anisotropy and heterogeneity. Across all CG types, the distribution of pores is uneven, with differences in pore size, shape, and connectivity. Intraparticle pores are a frequent feature of CG, often accompanied by blind pores on the surface or within the particle. However, the presence and development of through pores differ significantly among the different types of CG, which relates to the calcification and dissolution processes of CG and their skeletal structures. This observed heterogeneity in pore structure highlights the potential for variability in the mechanical and hydraulic properties of CG, especially under conditions of external stress or environmental changes such as particle breakage.

3.2 *Equivalent pore diameter distribution characteristics*

This section utilizes CT analysis to characterize the pores in CG before particle breakage. This analysis allows for a detailed understanding of the pore structure, which is crucial for assessing the potential behavior of CG in various applications. Figure 5 illustrates the cumulative pore volume (CPV) and pore size distribution (PSD) for each CG type.

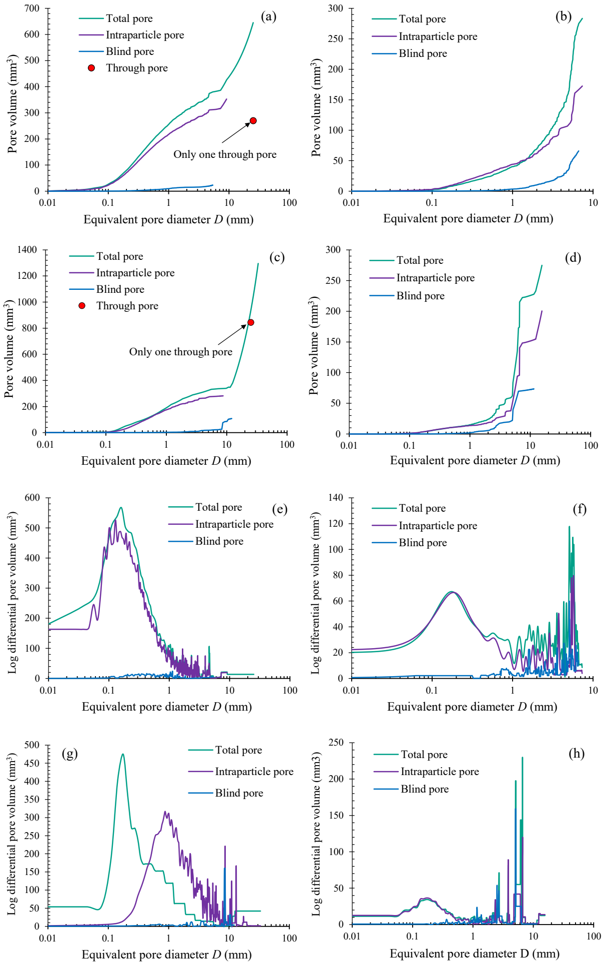

Figure 5. Results of CT tests on studied CG: the cumulative pore volume of (a) C1; (b) C2; (c) C3; (d) C4; and the pore size distribution (PSD) of (e) C1; (f) C2; (g) C3; (h) C4.

Porous features are prominently observed in rod-shaped CG (C1) and block-shaped CG (C3). Figures 5(a) and 5(c) indicate that both variants possess significant through pores, each with a diameter exceeding 10 mm. This characteristic substantially enhances the total pore volume, increasing the CPV curves. The through pore volume in C1 accounts for 41.84% of the total, whereas in C3, it comprises 68.4%. This indicates that these large pores significantly influence the pore structure of CG. In addition, the through pore volume in C3 is more than double that of C1, as demonstrated in the comparisons of their pore images in Figure 4.

The CPV curves of all CG samples reveal that although through pores are dominant, numerous smaller pores are also present. The PSD curves exhibit a skew toward smaller diameters, emphasizing a predominance of intraparticle and blind pores, which, despite their smaller size, collectively enhance the overall porosity. The distribution of blind and intraparticle pores shows consistent patterns across the CG types. Figure 5 illustrates that the volumes of blind pores in all four CG types are generally smaller than those of intraparticle and through pores, showing that blind pores are less significant in the total pore structure. Intraparticle pores exhibit a variety of sizes, with many being smaller. In the PSD curves (Figure 5(e)–5(h)), when the equivalent diameter is under 1 mm, the intraparticle pore curves of C1, C2, and C4 closely align with the total pore curve, indicating that these smaller pores are primarily intraparticle.

In addition, although branchlet and flaky CG lack through pores, they still display a distribution pattern with larger isolated pores contributing significantly to overall porosity. Particularly when the equivalent diameter surpasses 1 mm, the slope of the CPV curves for each pore type is shown in the Figures 5(b) and 5(d) increase markedly, and the PSD curves exhibit pronounced irregular peaks, indicating that these pores are more isolated and larger in volume at higher equivalent pore diameters. This is consistent with the pore morphology images shown in Figure 4. Pores in branchlet CG are more isolated and dispersed along the branches, with blind pores being prevalent. Numerous independent and large intraparticle pores and blind pores in flaky CG are evident (Figure 4), with intraparticle pore volume being the largest among the four CG types.

3.3 *Porosity characteristics*

Figure 6 and Table 1 reveal critical insights into the evolution of pore volumes and types across four coral gravel samples during simulation due to particle fragmentation, analyzed at different volume scales (1/1, 1/4, 1/9, and 1/16 of the single particle). A consistent trend is observed across all samples: relative intraparticle porosity decreases substantially as fragmentation progresses. This trend is particularly pronounced in the branchlet and flaky CG samples, where the initial relative intraparticle porosity exceeds 70%. Specifically, the intraparticle porosity of the branchlet CG decreases from 74.43% to 22.32% during particle fragmentation, while the flaky CG experiences a reduction from 72.88% to 12.2%. This decline is especially apparent between the 1/9 and 1/16 scales, indicating a threshold beyond which smaller particles experience a significant loss of internal pore structure.

Table 1. Porosity and relative porosity of CG at different scales.

Sample	Scale	Porosity				Relative porosity		
		ϕ_i (%)	ϕ_b (%)	ϕ_t (%)	ϕ_v (%)	f_i (%)	f_b (%)	f_t (%)
C1	1/1	4.92	0.32	3.77	9.02	54.62	3.54	41.84
	1/4	4.11	0.69	4.31	9.12	45.12	7.54	47.34
	1/9	3.40	0.96	5.00	9.35	36.36	10.23	53.41
	1/16	1.86	1.50	6.00	9.36	19.89	16.00	64.11
C2	1/1	6.91	2.37	0	9.28	74.43	25.57	0
	1/4	5.87	3.18	0.10	9.15	64.2	34.76	1.04
	1/9	4.21	4.54	0.56	9.32	45.2	48.75	6.05
	1/16	2.02	5.09	1.61	9.05	22.32	56.20	21.48
C3	1/1	4.70	1.80	14.06	20.56	22.85	8.75	68.40
	1/4	1.41	3.85	20.06	25.33	5.60	15.21	79.19
	1/9	0.522	4.29	29.55	34.36	1.52	12.49	85.99
	1/16	0.16	4.19	35.91	40.26	0.39	10.40	89.21
C4	1/1	3.70	1.37	0	5.07	72.88	27.12	0
	1/4	4.62	3.71	0.03	8.36	55.30	44.38	0.32
	1/9	3.01	3.90	0.04	6.96	43.30	56.06	0.64
	1/16	1.04	2.52	5.00	8.56	12.20	29.44	58.36

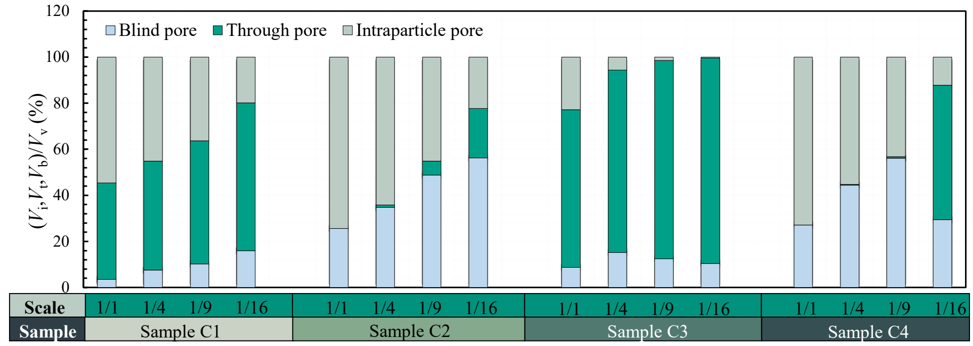

Figure 6. Results of relative porosity on various scales of CG: (a) C1; (b) C2; (c) C3 and (d) C4.

Simultaneously, the proportion of through pores increases as fragmentation intensifies, particularly between the 1/9 and 1/16 scales. This transformation exhibits a consistent trend across all CG types: intraparticle pores are gradually incorporated into larger, more interconnected through pores as fragmentation progresses. For example, this transformation is evident in the rod-shaped and massive CG samples, which already contain through pores in their initial volume states. The rod-shaped CG exhibits a uniform increase in relative through porosity throughout the fragmentation process. This is due to the evenly distributed intraparticle pores surrounding the through pores, enabling the gradual integration of intraparticle pores into the through pore network.

In the branchlet and flaky CG samples, which initially lack through pores, fragmentation reveals another significant trend: intraparticle pores gradually open and transition into blind and through pores as particle size decreases. Between the 1/9 and 1/16 scales, the proportion of blind pores increases substantially before eventually transforming into through pores. In the flaky CG, the increasing degree of fragmentation leads to numerous isolated intraparticle pores, which progressively connect and transition into through pores. This is reflected in the sharp increase in relative through porosity from 0.64% at the 1/9 scale to 58.36% at the 1/16 scale.

The pattern of pore evolution outlined above, particularly the development of through pores from initially blind and intraparticle pores, supports the hypothesis that CG becomes increasingly porous and interconnected as it fragments.

4 DISCUSSIONS

This study explores the pore characteristics of biogenic CG during particle breakage, encompassing fracture, crushing, and fragmentation processes. Pore composition remains a fundamental characteristic of coral particles and other construction materials. Although substantial research has concentrated on pore classification and morphology, the dynamic changes in pore structures during particle fragmentation have not been thoroughly explored. A multi-scale simulation framework was developed using X-ray computed tomography, enabling direct and consistent comparison of pore-scale changes among four typical CG types under identical fragmentation stages and flow conditions. Supported by CT imaging, this analysis uncovers consistent patterns of pore evolution throughout the fragmentation process, offering essential insights into how pore structures transform.

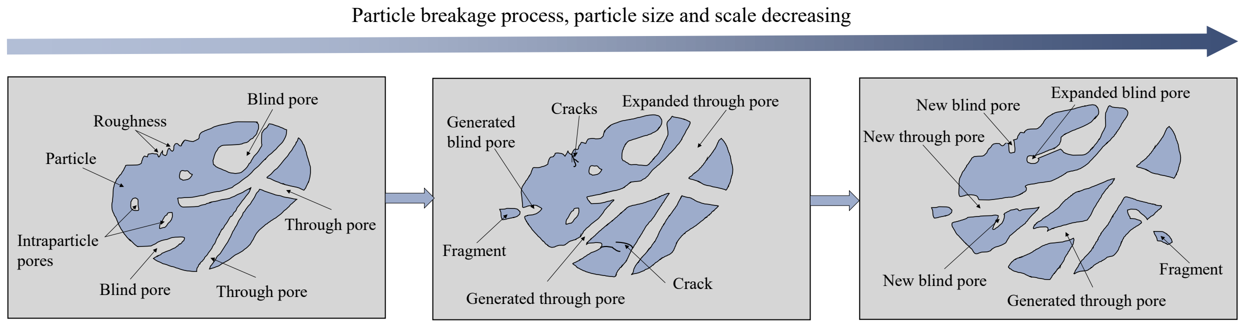

(a) Initial state (b) Slight breakage (c) Severe breakage

Figure 7. Schematic diagram of the evolution mechanism of various pores during particle breakage.

A model of the evolution of pore structures during particle fragmentation of CG is proposed through a representative progression, as illustrated in Figure 7. Based on the IUPAC classification, pores are categorized into three types: intraparticle, blind, and through pores. In the initial state (Figure 7(a)), intraparticle pores are situated deep within the particles, and surface roughness exists, facilitating the formation of cracks. During the early stages of particle breakage, depicted in Figure 7(b), cracks propagate from the surface inward under applied pressure, transforming intraparticle pores near the surface into blind pores. This behavior is particularly pronounced in samples with extensive internal pore networks, such as branchlet CG. The cracks fragment the inner pores, creating numerous blind pores, consistent with the observations in Section 3.3, where significant increases in blind porosity are recorded for branchlet CG and flaky CG. In addition, blind pores located near existing through pores can merge, enlarging the overall through pore volume. This mechanism clarifies the transformation of blind pores into through pores observed in the massive CG during fragmentation. As particle breakage intensifies, the pore structure undergoes further transformation. Figure 7(c) indicates that cracks propagate deeper, forming new blind pores while linking intraparticle and blind pores with existing through pores. This structural evolution becomes particularly pronounced at smaller scales, such as the 1/16 scale observed in flaky CG. At this stage, the proportion of blind pores can decrease as many merge into through pores. The extent of these changes largely depends on the initial pore distribution and the degree of fragmentation.

5 CONCLUSIONS

The main conclusions are as follows:

(1) CT technology is employed to characterize the morphology and pore structure of CG, identifying three types of pores: intraparticle, blind, and through pores. Rod-shaped CG and massive CG are characterized by prominent through pores; in rod-shaped CG, these are encircled by small intraparticle pores, while massive CG exhibits a complex structure with surface depressions and isolated blind pores. In contrast, branchlet and flaky CG are devoid of initial through pores. Branchlet CG displays intraparticle and blind pores along its branches, whereas flaky CG is predominated by calcareous cementation, featuring mainly intraparticle pores.

(2) Pore parameters such as pore diameter and porosity for various CG types are determined using 3D models. Porosity exhibits significant variation, with 20.56% in massive CG, whereas in the other three CG types, it does not surpass 10%. All CG types predominantly possess intraparticle pores. Intraparticle porosity in branchlet and flaky CG exceeds 70%, and collectively, CG displays higher intraparticle porosity than calcareous sands, with most pores being of small diameter.

(3) This research implements a multi-scale concept to simulate particle fragmentation and evaluate changes in porosity and permeability. Results indicated a marked reduction in intraparticle pores as fragmentation progresses. For instance, intraparticle porosity declined from 74.43% to 22.32% in branchlet CG and 72.88% to 12.2% in flaky CG. Simultaneously, the proportion of through pores increases between the 1/9 and 1/16 volume scales.

(4) This study provides a framework for clarifying pore evolution during particle breakage by analyzing shifts in porosity. As fragmentation advances, pore structure transitions from intraparticle and blind pores to through pores. Initially, intraparticle pores predominate, but surface fractures and crack propagation cause some to convert into blind pores, which later amalgamate with through pores. This dynamic is pivotal in forecasting the mechanical behavior of brittle geomaterials.

6 ACKNOWLEDGEMENTS

This work was supported by the National Natural Science Foundation of China (Grant No. 42372313) and the Fund of State Key Laboratory of Geomechanics and Geotechnical Engineering Safety, Institute of Rock and Soil Mechanics, Chinese Academy of Sciences (Grant No. SKLGME-JBGS2403).

7 REFERENCES

Clarkson, C.R., Solano, N., Bustin, R.M., Bustin, A.M.M., Chalmers, G.R., He, L., Melnichenko, Y.B., Radliński, A.P. and Blach, T.P. 2013. Pore structure characterization of North American shale gas reservoirs using USANS/SANS, gas adsorption, and mercury intrusion. *Fuel* 103, 606-616.

Coop, M.R., Sorensen, K.K., Bodas Freitas, T. and Georgoutsos, G. 2004. Particle breakage during shearing of a carbonate sand. *Géotechnique* 54(3), 157-163.

Ding, Z., He, S.H., Sun, Y., Xia, T. and Zhang, Q. 2021. Comparative study on cyclic behavior of marine calcareous sand and terrestrial siliceous sand for transportation infrastructure applications. *Construction and Building Materials* 283, 122740.

Fan, Z., Hu, C., Zhu, Q., Jia, Y., Zuo, D. and Duan, Z. 2021. Three-dimensional pore characteristics and permeability properties of calcareous sand with different particle sizes. *Bulletin of Engineering Geology and the Environment* 80, 2659-2670.

International Union of Pure and Applied Chemistry (IUPAC) Physical Chemistry Division Commission on Colloid and Surface Chemistry, Subcommittee on Characterization of Porous Solids. 1994. Recommendations for the characterization of porous solids (Technical Report). *Pure and Applied Chemistry* 66(8), 1739-1758.

Lyu, B.C., Wang, A.G., Zhang, Z.H., Liu, K.W., Xu, H.Y., Shi, L. and Sun, D.S. 2019. Coral aggregate concrete: Numerical description of physical, chemical and morphological properties of coral aggregate. *Cement and Concrete Composites* 100, 25-34.

Ni, X., Miao, J. and Lv, R. 2017. Quantitative 3D spatial characterization and flow simulation of coal macropores based on MCT technology. *Fuel* 200, 199-207.

Ouellet, S., Bussière, B., Aubertin, M. and Benzaazoua, M. 2007. Microstructural evolution of cemented paste backfill: Mercury intrusion porosimetry test results. *Cement and Concrete Research* 37(12), 1654-1665.

Shen, J., Xu, D., Liu, Z. and Wei, H. 2020. Effect of particle characteristics stress on the mechanical properties of cement mortar with coral sand. *Construction and Building Materials* 260, 119836.

Zhang, X.W., Liu, X.Y., Xu, Y.Q., Wang, G. and Zang, M. 2022. Fragmentation modes of single coral particles under uniaxial compression: Microstructural insights. *Construction and Building Materials* 344, 128186.